GCAGS JOURNAL
A Publication of the Gulf Coast Association of Geological Societies
www.gcags.org

Heterogeneity of Microscale Lithology and Pore Systems in an Upper Cretaceous Eagle Ford Group Horizontal Core, South Texas, U.S.A.

Robert M. Reed, J. Evan Sivil, Xun Sun, and Stephen C. Ruppel

Bureau of Economic Geology, Jackson School of Geosciences, University of Texas at Austin, University Station, Box X, Austin, Texas 78713, U.S.A.

ABSTRACT

A horizontal core from the Upper Cretaceous Eagle Ford Group of South Texas provides a rare opportunity to study lateral heterogeneity of lithology, total organic carbon (TOC), and pore systems in a calcareous-argillaceous mudstone from the subsurface. The core is 182 ft (55.5 m) long and spans between 2 and 4 ft (0.6 and 1.2 m) of stratigraphic section. True vertical depth is ~10,970 ft (~3343.7 m). Calculated vitrinite reflectance (R_o) is ~1.1%. Macroscopic variations in lithology are related primarily to foraminiferal abundance. Millimeter-scale grainstone laminae with numerous foraminifera are common but generally discontinuous.

On a microscopic scale, the rock can be divided into three major domains or lithologic components: coccolith-rich pellets, siliceous-argillaceous seams, and foraminifera. Pellets contain intraparticle pore spaces filled with organic matter interpreted to be migrated bitumen. Siliceous-argillaceous seams anastomose around the pellets and are predominantly clay minerals with quartz, albite, and minor organic matter. The ratio of siliceous-argillaceous seams to pellets varies between laminae and between samples. Macroscopically, there is variation in the abundance of foraminifera from sparse to abundant. Scanning electron microscope (SEM) examination shows chambers filled with calcite, kaolinite, and bitumen, along with minor pyrite, dolomite, and quartz. From sample to sample and from foraminifera to foraminifera, the proportion of fill material differs—some samples have more calcite, some more kaolinite, and some more bitumen. Chamber fill in grainstone laminae is dominantly calcite, and calcite cement is also present between foraminifera.

Variation also occurs in minor components of the samples. For example, differences in the abundance of originally siliceous, now pyritized radiolarians suggests local differences in the amount of dissolved silica available for quartz cement. Significant variations in the amounts of silt-size albite and dolomite occur between samples (e.g., some samples have twice the albite of others).

These rocks have a complex pore system. Within bitumen in pellets and foraminifera chambers there are typically two sizes of organic-matter pores: submicrometer-scale spherical to slightly elongate pores and more numerous nanometer-scale pores. The larger pores appear to be connected by the smaller, more numerous pores. Also a few early micrometer-scale pores were developed during initial migration of bitumen. Within the siliceous-argillaceous seams surrounding the pellets are nanometer-scale interparticle pores. As pore abundance is influenced primarily by the local ratio of pellets to siliceous-argillaceous seams, lateral variations in this ratio drive variations in the pore system.

INTRODUCTION

Much remains to be understood about small-scale heterogeneity in mudrocks and its influence on reservoir properties, including pore systems. This study aims to characterize variations in the pore systems and small-scale lithological differences within the length of a horizontal core.

The Upper Cretaceous (Cenomanian-Turonian) Eagle Ford Group of South, Central, and East Texas is a prominent calcareous mudrock unit and a prolific hydrocarbon reservoir. The Eagle Ford has been extensively studied across a variety of disciplines (e.g., Denne et al., 2014; Hentz et al., 2014; Eldrett et al., 2015; Breyer, 2016; Fairbanks et al., 2016; Milliken et al., 2016; Loucks, 2018), particularly where it serves as a hydrocarbon reservoir in South Texas. The unit is made up of beds of limestone, organic-rich calcareous-argillaceous mudstone, and altered volcanic ash, in varying proportions (e.g., Eldrett et al., 2015; Minisini et al., 2018). Previous microscopic studies on the

Manuscript received April 7, 2019; revised manuscript received July 15, 2019; manuscript accepted August 5, 2019.

GCAGS Journal, v. 8 (2019), p. 22–34.
DOI: pending

organic-rich beds (Reed and Ruppel, 2012; Pommer and Milliken, 2015; Schieber et al., 2016; Ko et al., 2017) have shown that pores in thermally mature mudrocks are present as organic-matter pores, interparticle pores, and intraparticle pores (Loucks et al., 2012). These studies report variability in the development of the three pore types with lithology and thermal maturity.

Horizontal cores are not commonly acquired in mudrocks. Access to a horizontal core in the Eagle Ford from a producing horizon provides a rare opportunity to study microscale lithology and pore systems in an argillaceous calcareous mudrock from the subsurface. Lateral changes of macroscale lithology seen in roadcuts (e.g., Frebourg et al., 2016) suggest that microscale features may change laterally as well.

SAMPLES AND METHODS

The Eagle Ford horizontal core for this study was acquired in Atascosa County, Texas, east of the Maverick Basin and south of the San Marcos Arch (Fig. 1). The core is 182 ft (55.5 m) long and spans between 2 and 4 ft (0.6 and 1.2 m) of vertical section, as will be discussed below. The landing zone is in the lower Eagle Ford Group approximately 60 ft (18.3 m) above the base at a true vertical depth of ~10,970 ft (~3343.7 m).

Macroscopic examination of the core showed variation from a calcareous argillaceous mudstone through wackestone to packstone (classification of Dunham, 1962) with visual variations being mainly related to foraminiferal abundance (Figs. 2 and 3). Thin white grainstone laminae with numerous pelagic foraminifera (primarily globigerinids) are common and seem to increase in number toward the toe of the core (Fig. 2). Thicknesses of the grainstone laminae are variable in the mm to sub-mm range, with thicknesses varying both between laminae and within laminae. Laminae are generally discontinuous at the centimeter scale. Low angle truncations against other laminae occur in some cases. Local thickening of the laminae may indicate small scours.

Scanning electron microscope (SEM) samples were prepared for examination using broad ion-beam (BIB) milling with argon ions. Samples were processed using a Leica EM Triple Ion-Beam Cutter (TIC) 020 system. Samples were ion-milled using an accelerating voltage of 8 kV, a source current of 2.8 mA, and a milling time of 10 hr. Milled surfaces were cut perpendicular to bedding. All BIB samples were given an ~6 nm coating of iridium to prevent charge buildup during SEM examination. BIB samples were imaged using a field-emission SEM; an FEI Nova NanoSEM 430 model equipped with dual Bruker XFlash® SDD energy dispersive spectroscopy (EDS) systems for element identification and mapping. A moderate accelerating voltage of 15 kV was used on this system to avoid causing electron beam damage to the samples while still allowing efficient EDS measurement. SEM working distances for imaging were ~6 mm and for EDS mapping were 9 to 10 mm. SEM images and EDS element maps were collected from all samples. Twenty-one samples from six different vertical slices distributed along the length of the core were selected for SEM study and organic geochemical analyses.

Organic geochemical samples were ground into powder and part of the powders were treated with dichloromethane to dissolve bitumen. Then the treated samples were sent to Geomark Research (Humble, Texas) for LECO TOC and RockEval analy-

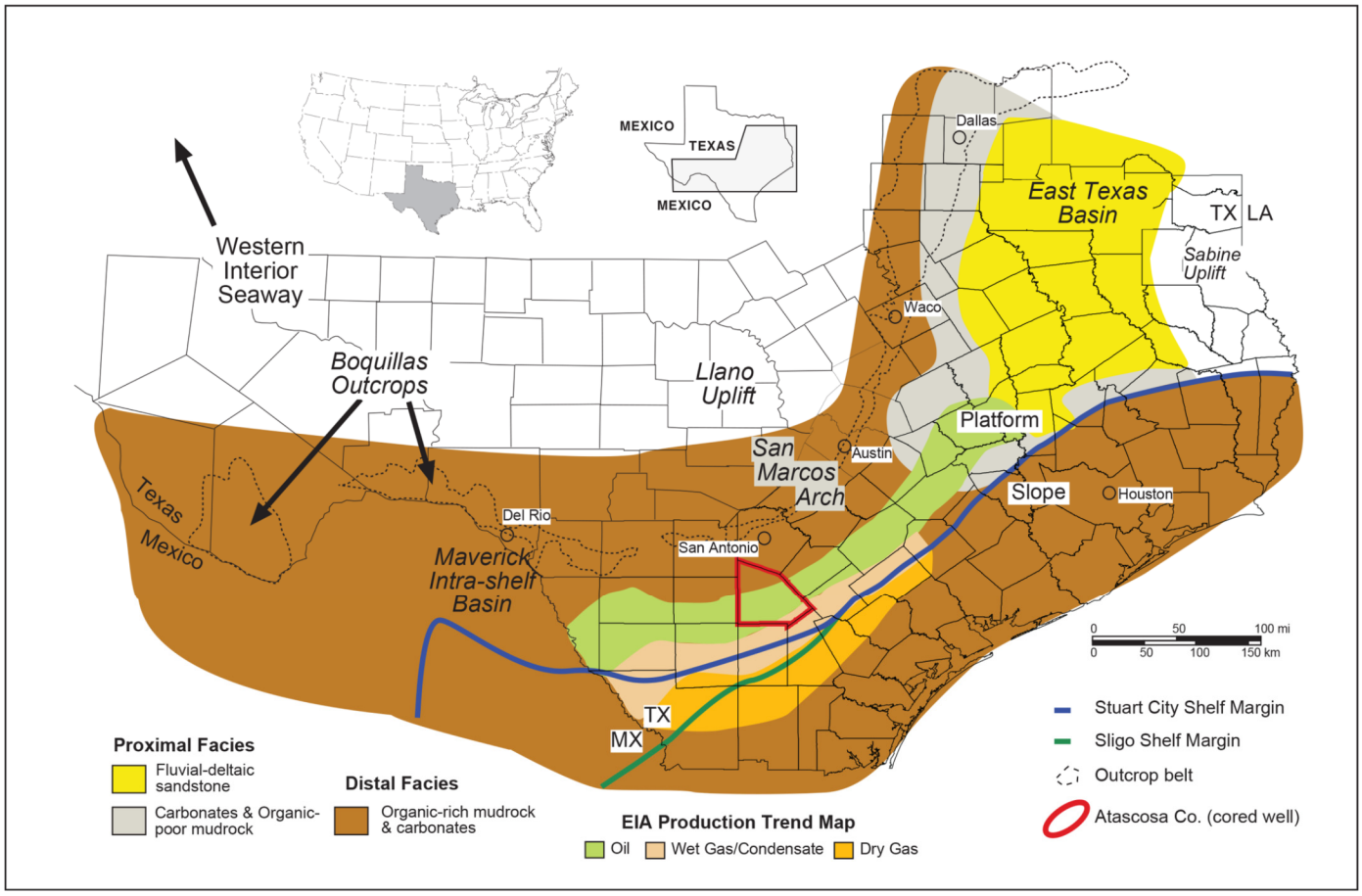

Figure 1. Paleogeographic map of the late Cenomanian showing the distribution, production trends, and facies of the Eagle Ford Group and equivalent units in Texas (modified after Ruppel et al., 2012). Major structural features are also marked. Inset map shows the location of Texas in the United States of America.

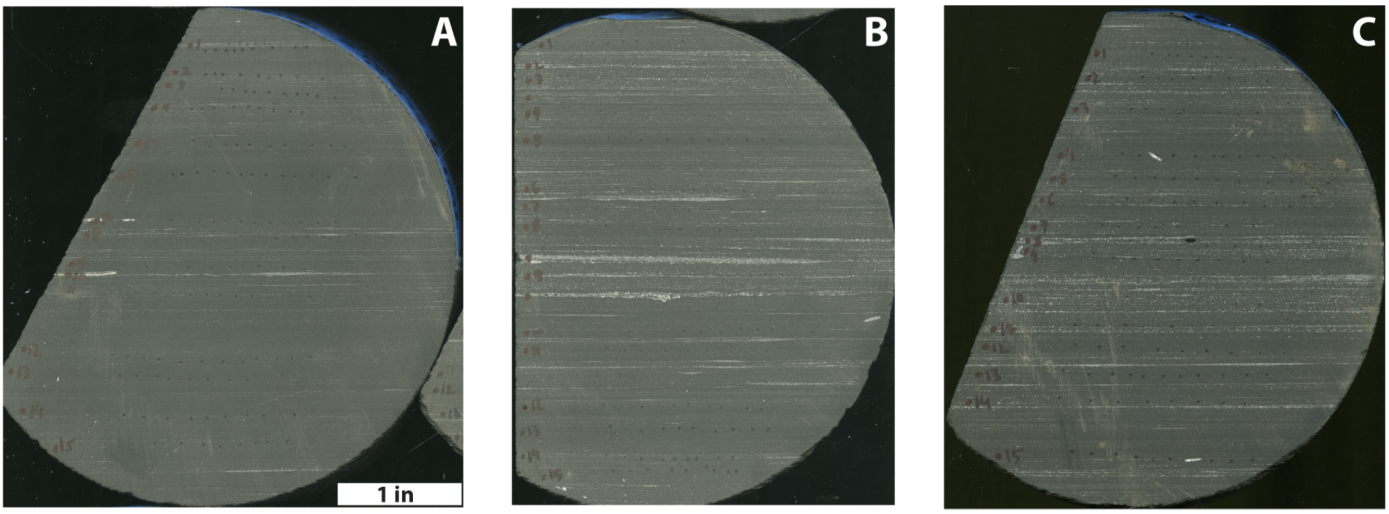

Figure 2. Photographs showing three of the vertical core slices used in this study. A is slice 1, B is slice 4, and C is slice 6. Note the increase in lighter color, foraminifera-rich laminae to the right (toward the toe of the core). Core diameter is 4 in (102 mm). Numbers and red spots indicate the location of micro-rebound hammer measurements on the core.

sis. Non-extracted RockEval and TOC data were provided by the operator who acquired the core.

Energy-dispersive X–ray fluorescence (XRF) data were collected at a 2 mm spacing on vertical core slices using a Bruker Tracer IV handheld XRF unit attached to a DeWitt MCS–1000E Model T1 automated core scanner. The automated core scanner used a step motor to ensure that samples were scanned for 14 major and 16 trace elements in the same locations. Due to the varying sample size, each core slice was scanned, on average, at 50 locations for major elements and 50 locations for trace elements. A total of 40 vertical core slices were scanned by XRF from the 182 ft (55.5 m) length of core.

The six vertical core slices taken for organic geochemical and SEM analyses were subjected to more extensive XRF scanning. Element maps for the samples (Fig. 3) were made by Bruker using a Bruker M4 Tornado XRF mapping system. The Tornado uses a microbeam X–ray fluorescence (Micro–XRF) rhodium (Rh) tube that was excited to a voltage of 50 keV with a current of 600 µA and read using dual 60 mm2 XFlash silicon drift detectors. Samples were polished and placed level within the vacuum chamber of the Tornado on the sample stage which moves over the X–ray tube and detector. For this study samples were analyzed at a spot size of 60 µm per pixel and over 20 million scans were collected at 4 ms/pixel. Each sample analyzed took ~6 hr.

RELATION OF HORIZONTAL CORE TO BEDDING

Macroscopic examination of the core shows that it is located almost entirely in one lithology, a calcareous argillaceous mudstone or "marly" bed. Within this overall lithology there are more argillaceous laminae and more calcareous laminae (Fig. 2). No macroscopically visible faults were noted in the core. None of the limestone or volcanic ash beds that are known to occur in the Eagle Ford in this unit (e.g., Eldrett et al., 2015; Pierce et al., 2016; Ko et al., 2017; Minisini et al., 2018) were sampled in the core. This provides a preliminary constraint on the thickness of the cored interval. The report from the contractor that acquired the horizontal core estimated that the depth variation was approximately 4 ft (1.2 m) at a true vertical depth of ~10,970 ft (~3343.7 m). To further constrain depth variation, after the detailed XRF analysis of 40 vertical core slices, the slices were correlated based on variations in the chemical makeup of the laminae using multiple chemical elements. This correlation shows some vertical changes in the position of the core relative to laminae within the bed. Assuming the correlation is correct, the stratigraphic interval sampled by the core is less than 2 ft (0.6 m) thick.

TOTAL ORGANIC CARBON AND PROGRAMMED PYROLYSIS MEASUREMENTS

LECO TOC measurements, supplied by the operator for samples taken along the length of the core, vary from 4.2 to 6.0% and average 5.0%. Post-bitumen-extraction LECO TOC measurements vary from 3.4 to 5.4% and average 4.4%. When either set of values for TOC is plotted versus length along core there are some fluctuations, but the general trend is for a slight decrease in TOC toward the toe of the core. Decreasing TOC is also weakly correlative with an increase in carbonate content.

RockEval pyrolysis results from samples taken along the length of the core were available from the operator. RockEval maximum temperature (T_{max}) of the S2 peak (representing petroleum produced form kerogen during thermal pyrolysis) averages 446.1ºC (835.0ºF) for these samples. However, the pyrograms from these samples suffered from consistent low–T shoulders on the S2 peaks because of retained hydrocarbons. Low–T shoulders on the S2 peaks are known to cause lowering of T_{max} values which leads to an underestimation of thermal maturity (e.g., Abrams et al., 2017). As stated above, for this study powders of the 21 samples were treated with dichloromethane to remove bitumen prior to a second series of programmed pyrolysis measurements. Post-extraction RockEval T_{max} for the samples shows no low–T shoulders on the S2 peaks and averages (459.1ºC) (858.2ºF). Using the conversion formula of Jarvie et al. (2001), this T_{max} gives a calculated vitrinite reflectance (R_o) of ~1.1%.

XRF OBSERVATIONS

XRF maps produced by the Bruker M4 Tornado are available for the 6 vertical slices through the core that were subsequently used for SEM samples and organic geochemistry studies (Fig. 3). Thirty-one element maps, covering major and trace elements, were made for each vertical slice. Elemental abundances are expressed as color intensities, with high concen-

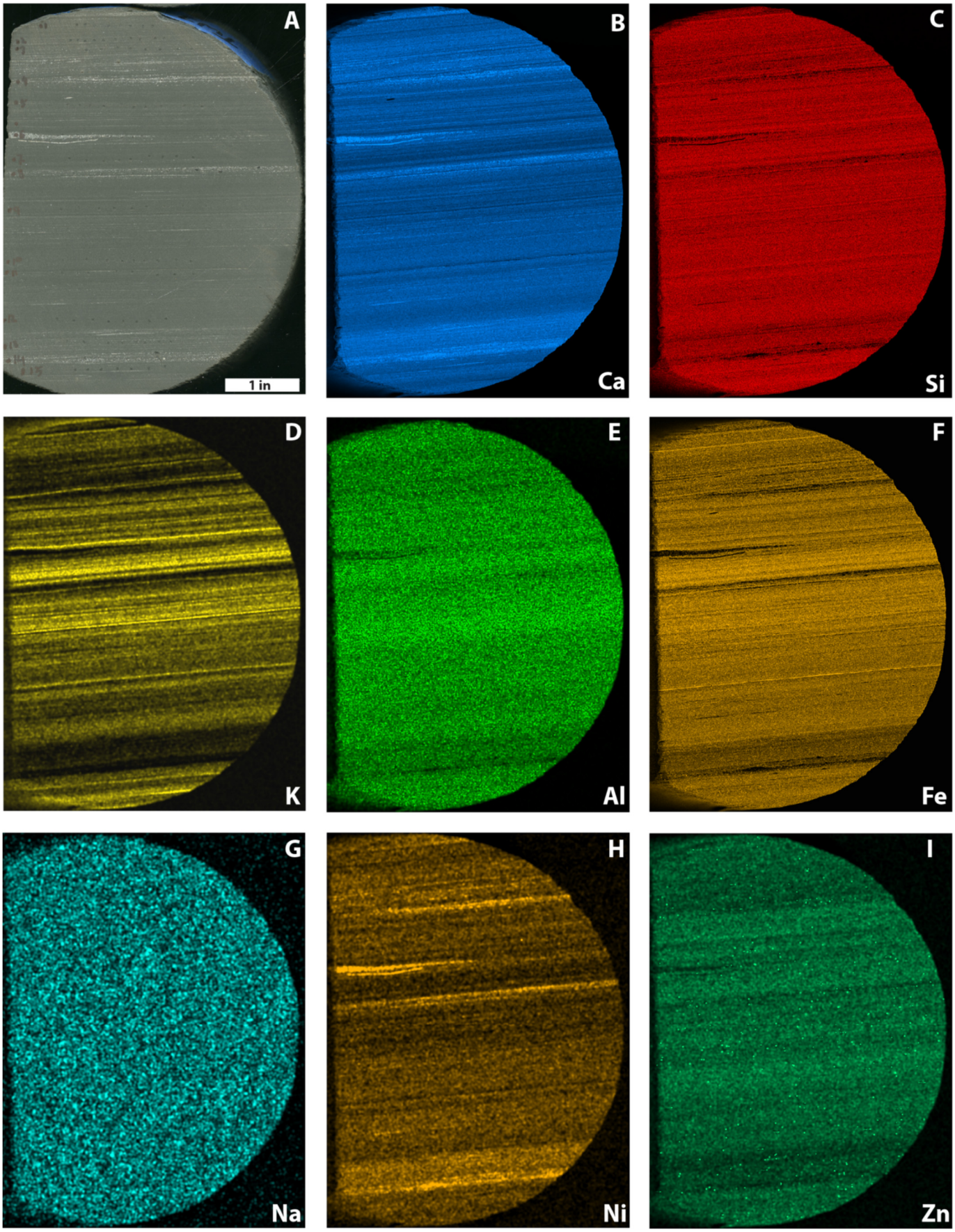

Figure 3. Photograph and XRF scans of vertical slice 3 through the horizontal core. Core diameter is 4 in (102 mm). (A) photograph of the core slice and XRF intensity maps for (B) calcium, (C) silicon, (D) potassium, (E) aluminum, (F) iron, (G) sodium, (H) nickel, and (I) zinc. Note the variation in laminations or lack of laminations between elements.

trations expressed as brighter colors. Elemental intensities are normalized to the highest concentration of that element in a sample.

Major elements show either intensity laminations, varying from strong (Fig. 3D) to moderate (Fig. 3E), or a more homogeneous speckled pattern of occurrence (Fig. 3G). Calcium shows one of the most strongly laminated fabrics (Fig. 3B) and also picks out the rare occurrence of mollusk shells in some of the slices. Silicon shows relatively weaker laminations (Fig. 3C), which are generally the inverse in intensity of the laminations shown by calcium. Potassium shows strong laminations that generally match those shown by silicon (Fig. 3D) but are more negative in intensity in the calcium-rich laminae than silicon. Aluminum shows a few faint laminae that also reflect more intense silicon layers, but aluminum has a strong speckled pattern as well (Fig. 3E). Phosphorous shows only a few strong laminations which correspond with high calcium and low silicon layers. Iron maps show strong laminae patterns (Fig. 3F) which are very similar to the silicon element maps, except a few of the highest intensity iron laminae are less strongly developed in the silicon maps. Manganese shows a lamination that is virtually identical to iron and is the inverse of calcium. Sodium is notable among the major elements for not showing any laminations, but instead showing a speckled pattern of high intensity points (Fig. 3G) which may reflect a uniformly dispersed sodium-bearing phase or may reflect difficulties with light-element detection by the instrument. Magnesium is somewhat similar to sodium in generally lacking lamination, but some of the core slices show some faint positive intensity layers that correspond to higher calcium layers. Titanium shows laminae that generally correspond in intensity and position with the iron laminae, but a few core slices show one or more high intensity grains that reflect XRF peak interference from barium (see below). Sulfur shows a few negative intensity laminae that correspond with high calcium laminae, and a few bright laminae that correspond with the brightest laminae in the iron maps. A few millimeter-scale spots of high sulfur are also correlated with high barium (see below).

For the trace elements, only those maps that showed a definitive pattern will be discussed in detail. In three of the core slices, the presence of millimeter-scale barite (?) grains mostly overwhelms a faint lamination pattern seen in the other barium maps. The barium lamination is the inverse of the calcium lamination (Fig. 3B). Chromium, manganese, and vanadium maps show a fainter version of the iron lamination pattern (Fig 3F) and are the inverse of the calcium pattern. Cobalt shows a few faint laminations; the pattern appears to be the inverse of the calcium pattern. Copper is inconsistent in behavior between core slices. Some slices show a few faint copper laminations, of either positive or negative intensity, and some slices show no lamination at all. Gallium shows the faintest, most diffuse laminations of any element mapped. Nickel shows virtually the same pattern of laminae (Fig. 3H) that is seen in calcium maps (Fig 3B) only not as well developed. Some niobium maps show faint laminae, but others do not. Molybdenum and rubidium both show a few faint low intensity laminae in a background of higher intensity areas; the low intensity laminae correspond with high calcium laminae. Strontium shows relatively strong laminae that share a pattern with calcium. The yttrium maps show some of the same high intensity layers picked out by the phosphorous maps. Zinc shows both a faint lamination that is the inverse of the calcium laminations and also a few bright spots (Fig. 3I) that suggest the presence of grains of a zinc-rich mineral (probably sphalerite). Zirconium shows a few faint negative intensity laminae, which correspond with low iron and high calcium layers.

The trace elements arsenic, bromine, cadmium, lead, selenium, thorium, and uranium were mapped, but these did not show any laminations or other clear patterns. It is unclear if this represents a relatively homogeneous distribution of these elements, or these elements being generally below detection limits in the samples, or possibly insufficient count times to accurately detect low concentration elements.

In terms of variability along the length of the core, some patterns are apparent. As previously noted, calcite-rich and hence calcium-rich laminae increase towards the toe of the core (Fig. 2). Elements that seem to have similar patterns of occurrence to calcium (e.g., nickel and strontium) show the same increase in high intensity laminae toward the toe of the core. Elements with negative correlation with calcium (e.g., iron and silicon) show a decrease in high intensity laminae toward the toe of the core. The occurrence of phosphorous-rich layers is highly variable from vertical slice to vertical slice, but there is no clear trend to the changes.

MICROSCOPIC OBSERVATIONS

On a microscopic scale, the rock can be divided into three major domains; coccolith-rich lenses (compacted pellets), siliceous-argillaceous seams, and foraminifera (Fig. 4). These domains are small scale areas of distinct grain, cement, and organic matter assemblages that also show distinct pore systems. Important minor components outside the domains include pyritized radiolarians, phosphatic material of various types, feldspar grains, quartz, and dolomite.

Coccolith Pellets

Coccolith-rich pellets are a common and typically abundant component in the samples (Fig. 4), and pellet density is highly variable in the samples. Pellet lengths are in the tens of micrometers range. Pellet thickness varies from pellet to pellet, but aspect ratios are greater than 3:1. Although the original, precompaction pellet shapes are thought to have been elongate (e.g., Dagg and Walser, 1986), present shapes are elongate parallel to bedding and show evidence for compaction, including deformation around rigid foraminifera tests. Intraparticle pore spaces between coccolith fragments are filled with what is interpreted to be migrated bitumen (Loucks and Reed, 2014, Milliken et al., 2014). This varies from the pellets (i.e. coccolith hash) described by Ko et al. (2017) in which some of these intraparticle spaces are free of bitumen. Minor euhedral quartz grains (probably quartz cement) occur in the pellets as well.

Siliceous-Argillaceous Seams

Siliceous-argillaceous seams anastomose around the coccolith-rich pellets and the foraminifera. These areas are predominantly clay minerals with quartz, albite feldspar and minor organic matter (Fig. 4). Quartz is present in these samples both as typically rounded, silt-size grains (probably detrital) and as smaller more euhedral grains that are at least partly quartz cement. This observation is similar to Milliken et al. (2016) findings on the nature of quartz grains in the Eagle Ford. Dolomite is present in these seams as well, down to clay size.

Intact coccoliths are very rare in these samples, but disaggregated coccolith elements are commonly found mixed into these seams.

Foraminifera

The foraminifera in the samples are dominantly pelagic forms, principally globigerinids. Macroscopically there is variation in the abundance of foraminifera from abundant (grainstone) through widely dispersed (wackestone). SEM examination shows another variation; foraminifera chamber fill includes calcite, kaolinite, bitumen and less commonly quartz, pyrite and dolomite (Fig. 5). Little of the original intraparticle pore space is preserved, as will be discussed in the section on pores. Many foraminifera show different fill material in different chambers.

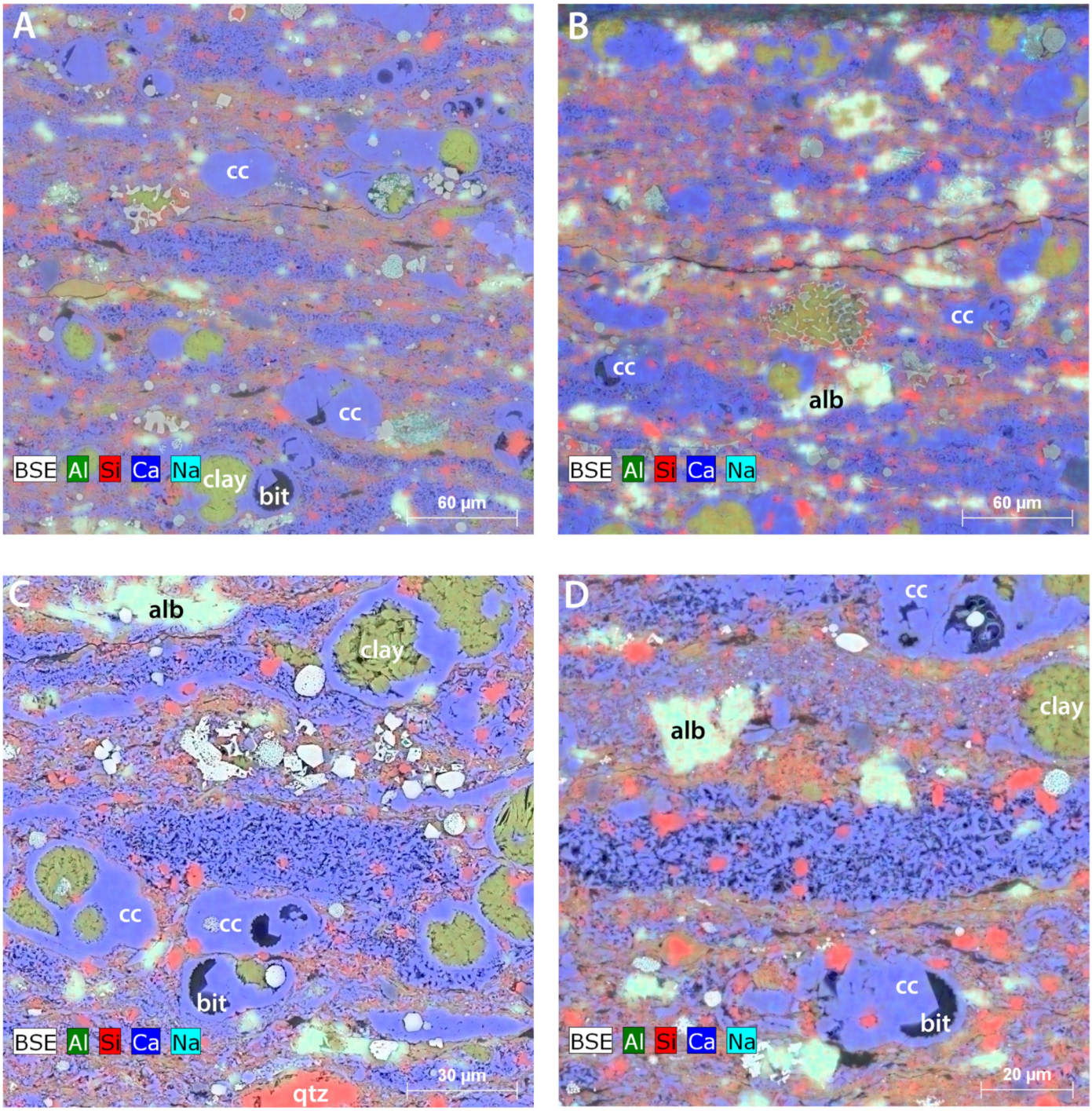

Figure 4. Color energy dispersive spectroscopy (EDS) element maps (aluminum is green, silicon is red, calcium is dark blue, and sodium is aqua) superimposed on backscattered electron SEM images. In all, red is quartz (qtz), blue is predominantly calcite (cc), green is clay minerals including kaolinite, aqua is albite (alb), black is organic matter (bit indicates bitumen), and light gray is mostly pyrite (pyr). (A) Lower magnification image showing foraminifera, coccolith-rich lenses (pellets), and siliceous-argillaceous seams. (B) Lower magnification image showing an albite-rich area of a sample. (C) Higher magnification image showing a coccolith-rich lens with migrated bitumen between the disaggregated coccolith elements in the pellet. (D) Another higher magnification image showing an elongate coccolith-rich lens (center).

The timing of fill is not entirely clear, but mineralization by calcite, pyrite, quartz, and kaolinite all took place before migration of bitumen. Calcite precipitation appears to have been early and predates both quartz and kaolinite precipitation. Dolomite appears to have replaced kaolinite and possibly calcite. From sample to sample and from foraminifera to foraminifera, the proportion of fill material changes; some samples have more calcite, some more kaolinite, some more bitumen. Adjacent foraminifera can have different proportions of fill.

One sample examined was from one of the millimeter-scale grainstone laminae. These are composed primarily of foraminifera, typically the larger specimens. SEM imaging showed that the foraminiferal chamber fill for this layer is dominantly calcite. Calcite cement is also present between foraminifera.

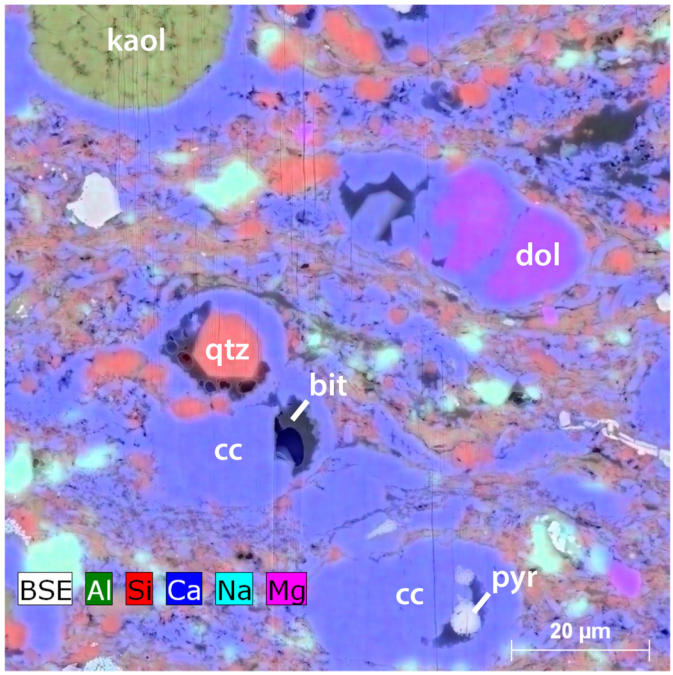

Figure 5. Color EDS element maps (aluminum is green, silicon is red, calcium is dark blue, sodium is aqua, and magnesium is magenta) superimposed on a backscattered electron SEM image. Image shows the five mineral phases that fill foraminifera chambers in these samples; calcite, kaolinite, quartz, dolomite, and pyrite. Same color scheme for minerals as Figure 4 with the addition of purple for dolomite.

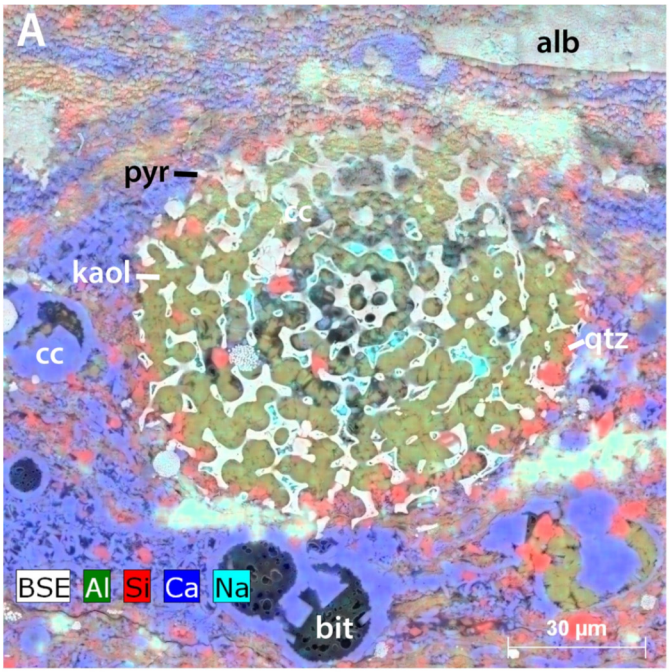

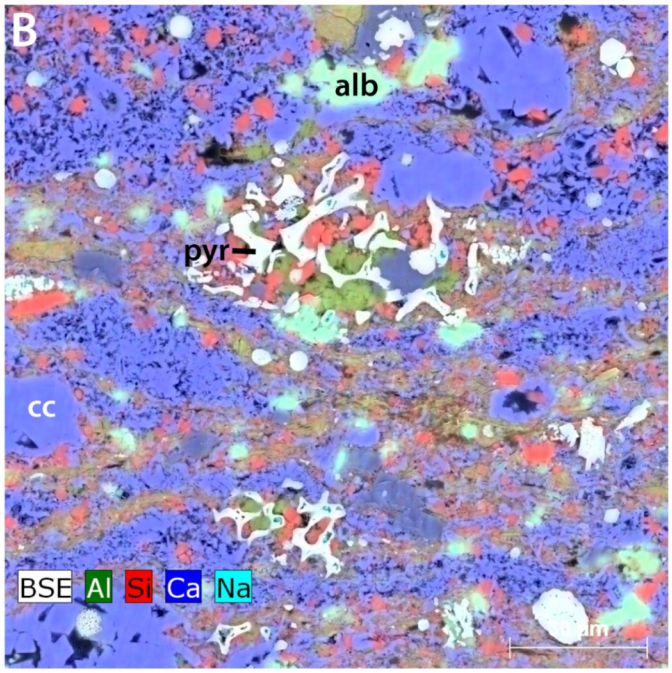

Figure 6. Color EDS element maps (aluminum is green, silicon is red, calcium is dark blue, and sodium is aqua) superimposed on backscattered electron SEM images. (A) A relatively complete pyritized radiolarian with interstices filled with kaolinite (green), quartz (red) and bitumen (black). (B) Partially preserved pyritized and broken radiolarians. Color scheme for minerals is the same as Figure 4.

Radiolarians

Commonly present although not abundant in the samples are originally siliceous radiolarians replaced by pyrite (Fig. 6), a phenomenon which was previously described in the Eagle Ford by Milliken et al. (2016). In the samples examined, pyritization is the only replacement method seen for radiolarians. The replaced radiolarians are typically only partially preserved and commonly show evidence for compaction. A progressive sequence is present from almost completely preserved radiolarians (Fig. 6A) to highly disaggregated radiolarian debris (Fig. 6B). This allows for the highly disaggregated material to be recognized as the remnants of radiolarians. Original intraparticle pore spaces in the radiolarians are commonly filled with kaolinite and more rarely with quartz, dolomite, and bitumen (Fig. 6A). The abundance of radiolarians varies between samples and areas within samples, which leads to variation in the amount of silica that was locally available for the formation of authigenic quartz cement. Radiolarians appear to be more abundant in samples with more foraminifera.

Organic Matter

The distribution and mode of occurrence of organic matter has been partially discussed in other sections of this work, but will be more fully described here. The chambers of foraminifera commonly contain migrated organic matter (bitumen). In some chambers, bitumen is the dominant pore-filling phase. In some chambers, bitumen is secondary to calcite or kaolinite cement (Fig. 5). In some fields of view bitumen is the dominant fill type, but in other fields of view bitumen is practically absent. Similar to foraminifera, but in much lower volumes, migrated organic matter can be found partially filling in the interstices of pyritized radiolarians (Fig. 6A).

At one point, coccolith pellets contained abundant intraparticle porosity, with pores occurring between the coccolith fragments in the pellets. Currently, these spaces are filled with abundant migrated organic matter (bitumen).

Large organic-matter masses, where the organic matter is mixed with clay-size mineral grains, are fairly common within the samples and occur within the siliceous-argillaceous seams. These masses are elongate parallel with layering and have varia-

ble but high aspect ratios. Lengths can be up to sand size. Although there is some evidence for minor compaction of these masses, the original shape was probably elongate. These masses are interpreted to be kerogen.

Granular organic matter of silt size or larger that is not mixed with mineral matter is rare in these samples. These grains occur in the siliceous argillaceous seams that surround the coccolith pellets and not in the pellets. Some of these grains show cellular textures suggestive of plant material. This organic matter is likely kerogen rather than bitumen. These grains show little evidence of thermal alteration, leading to the interpretation that they may be less reactive type III or IV kerogen.

Phosphate

Calcium phosphate occurs in numerous forms in the samples from this study. Circular to elliptical phosphatic grains or nodules are present in some samples but are most common in grainstone laminae. These grains are up to sand size and commonly are concentrically zoned.

Also present are numerous phosphatic fossils, typically coarse silt to very fine sand size. Some of these fossils are wholly phosphatic (probably fish bones). Other fossils are lenticular, up to sand size, and are made up of phosphate mixed with organic matter on the nanometer-scale (probably fish scales).

An unexpected observation was the presence of numerous silt-size euhedral apatite crystals within the samples (Fig. 7). These crystals show little evidence for transport. Minor occurrences of diagenetic apatite are also present, typically as replacement of calcite adjacent to detrital apatite crystals.

Feldspar

Feldspar grains are common in the samples, but abundance varies dramatically from sample area to area (Fig. 4A versus Fig. 4B). Grains vary from fine silt to very fine sand size (Fig. 8A). In general, feldspar grains are larger in size than the detrital quartz grains present in these samples. Original feldspar composition is unclear, but as is common in thermally mature mudrocks (e.g., Milliken, 1992), the original composition feldspars have been replaced primarily by albite feldspar. Partial replacement of some feldspar grains by dolomite also occurs.

Quartz

These samples show the range of modes of occurrence that quartz can take on in a mudrock. Silt-size, rounded quartz grains of probable detrital origin are present in the siliceous-argillaceous seams. Smaller more euhedral quartz grains down to clay size present in the seams and in the pellets are interpreted to be wholly or partially authigenic in origin. Authigenic euhedral quartz cement is present in some foraminifera chambers and to a lesser extent in some radiolarian tests.

PORE SYSTEMS

The samples from the cored interval have complex pore systems (Fig. 9). As previously noted, there is abundant bitumen in the both foraminifera chambers and between the coccolith fragments in pellets. Within the bitumen there can be three sizes of organic-matter pores. The largest organic-matter pores are relatively rare, up to several micrometers in diameter, and generally spherical. In some cases, these pores take up most of a foraminifera chamber (Fig. 9A) and they tend to occur one organic-matter pore to chamber. Also present in the cavity-filling bitumen are spherical to somewhat elongate pores mostly in the hundreds of nanometer-diameter size range. In some cases, these pores appear to have formed through merging of smaller pores during pore expansion (Fig. 9B) The most numerous organic-matter pores in the bitumen have nanometer-scale diameters (Fig. 9C). These small pores are equant to elongate, with the larger pores being more commonly elongate. Bitumen typically contains a bimodal size distribution of organic-matter pores. The three different pore types are thought to have different formation mechanisms, and as these pores are formed in bitumen, all three types are connected in different ways to thermal maturation of the organic matter in the rocks.

Little of the organic matter in these samples occurs in sand- or silt-size granular forms, which are interpreted as kerogen (Loucks and Reed, 2014). A few pores occur in some of the ker-

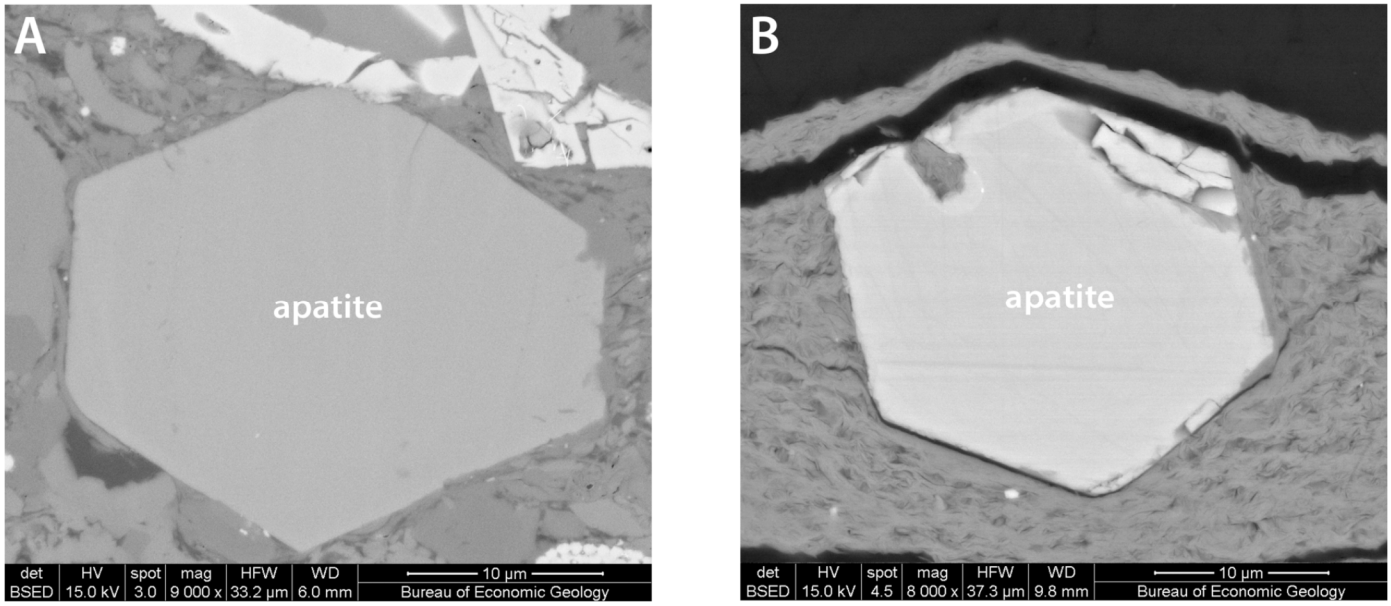

Figure 7. Backscattered electron SEM images of apatite crystals. (A) Euhedral apatite crystal from Atascosa County horizontal well. Such crystals are common in the samples from this study. (B) Euhedral apatite crystal from thin section of Karnes County volcanic ash layer.

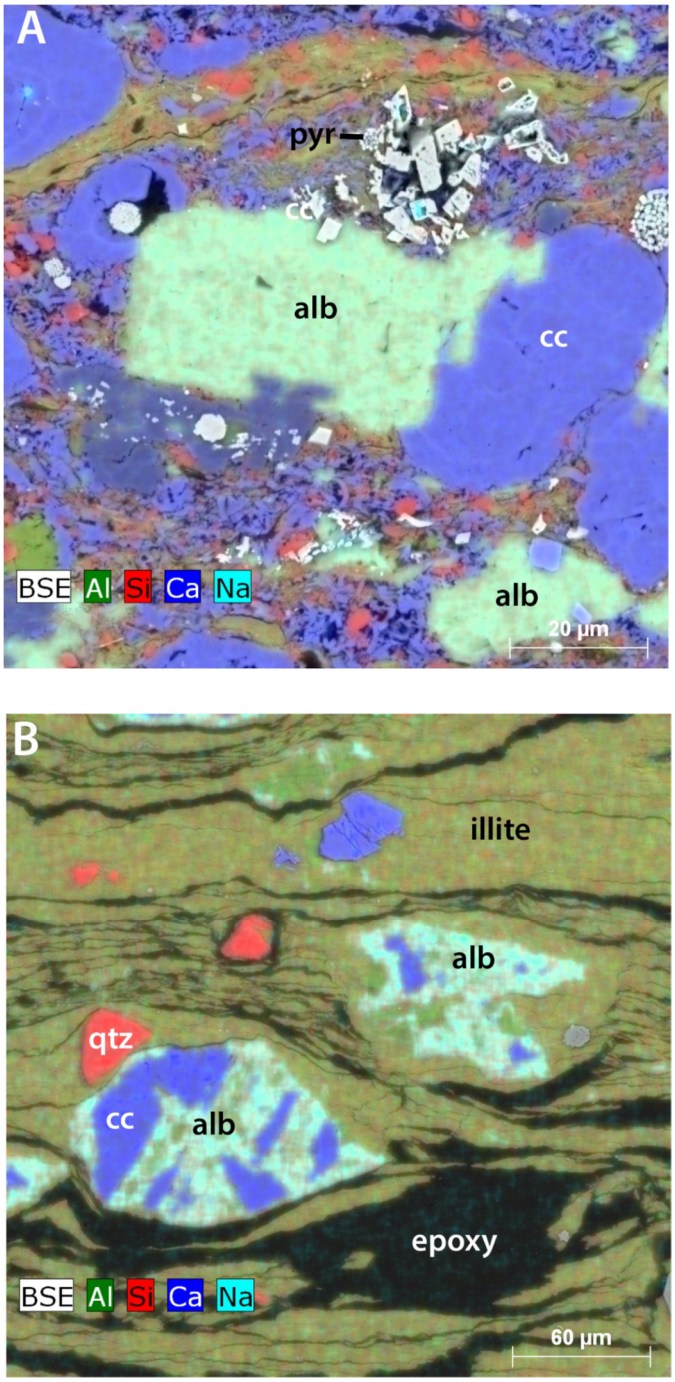

Figure 8. Color EDS element maps (aluminum is green, silicon is red, calcium is dark blue, and sodium is aqua) superimposed on backscattered electron SEM images. (A) Silt-size albite grains from Atascosa County horizontal well. These grains are common within samples from this study. (B) Silt- to sand-size albite grains partially replaced by calcite from thin section of Karnes County volcanic ash layer.

ogen grains and are probably predepositional in origin (Reed, 2017). Much of the identifiable kerogen in these rocks occurs as elongate silt- to sand-size masses mixed with mineral grains. These mat-like masses are typically non-porous.

The pores within the siliceous-argillaceous seams are primarily interparticle pores (Fig. 9D). These pores are between clay-mineral grains but also occur adjacent to silt-size quartz and feldspar grains. Pore shape is typically elongate or triangular. Sizes range from nanometer-scale to rarely micrometer-scale.

The core contains numerous but discontinuous grainstone laminae (Fig. 2), which are rich in foraminifera. Owing to the dominance of calcite cement both inside and outside of the foraminifera, pores of any type are rare in these laminae.

Intraparticle pores are present in a variety of grains (see below) but appear to contribute little to the overall pore system of the rock being involved more in storage than flow. Rarely intraparticle pore space in foraminifera chambers is preserved, but only in chambers mostly filled with kaolinite. Numerous lenticular organic-phosphatic fossils (probably fish scales) typically have nanometer-scale pores. Replacement of feldspar grains by albite is in some cases incomplete, leaving up to micrometer-scale pores in these grains.

MACRO- AND MICROFRACTURES

Macroscopic examination of the core revealed no macrofractures interpreted to be naturally occurring (i.e., none of the fractures present in the core contained visible syn- or post-kinematic cement). As previously noted, no faults were observed either.

Naturally occurring microfractures are generally thought to be uncommon in mudrocks (Gale et al., 2014; Loucks and Reed, 2016), but naturally occurring, horizontal bitumen-filled microfractures have been observed (Lash and Engelder, 2005). Samples from this horizontal core have more naturally occurring microfractures than is typical in mudrock samples. Five samples from four different vertical cuts have one or more naturally occurring microfractures, but most samples do not. These microfractures are subhorizontal and bitumen-filled (Fig. 10). Lengths can be at least a millimeter (some microfractures extend beyond edge of milled area), and apertures are up to several micrometers. Some of these microfractures have an en échelon arrangement. Post-coring deformation, possibly stress release, has partially reactivated most of them. Subhorizontal microfractures lacking bitumen and/or any mineral fill are more common and are interpreted to be post-coring in origin (Loucks and Reed, 2016).

DISCUSSION

Pore Systems

Pore systems in these samples are similar in many ways to those described by Ko et al. (2017). The exception would be one variety of their "modified mineral pores" which this publication prefers to classify as "early bitumen pores," a type of organic-matter pore.

Early bitumen pores (Fig. 9A) form at relatively low thermal maturity, when bitumen first begins to displace formation water in the surrounding pore space. The hypothesis is that in some pores, particularly foraminiferal chambers, the bitumen only displaces part of the water. The remaining water is left as a sphere surrounded by bitumen. These pores can be preserved to higher thermal maturities and may in later stages contain hydrocarbons. Large sizes (>1 µm) and occurring one to an original mineral pore are diagnostic of this pore type. In some cases, such as within coccolith pellets, these early bitumen pores can be difficult to distinguish from organic-matter bubble pores.

Bubble pores can also be a micrometer or more in diameter. The best way to discriminate early bitumen pores from bubble pores is that bubble pores can show evidence of formation by coalescence of smaller bubble pores as they grow (Fig. 9B). Also, in a large original mineral pore, such as a foraminifera chamber, numerous bubble pores will form in bitumen (Fig. 9B) whereas smaller numbers of early bitumen pores form (typically one). We hypothesize that these large bubble pores may form through the breakdown of bitumen to form oil. It is thought that these pores begin to form around 0.75% R_o (Reed and Ruppel, 2012; Pommer and Milliken, 2015).

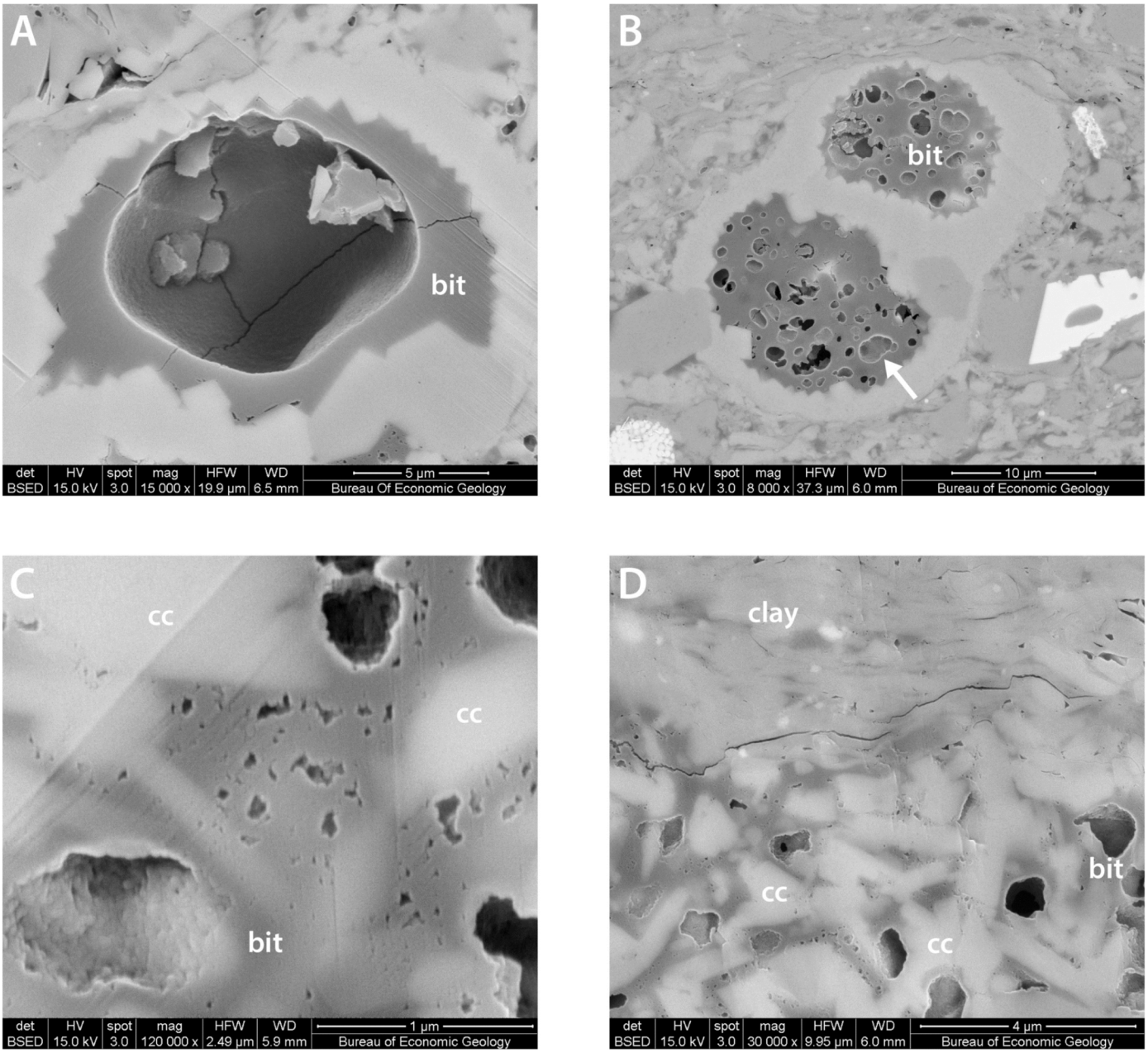

Figure 9. Backscattered electron SEM images of various pore types from samples. (A) Image showing a single large organic-matter pore (early bitumen pore) in a foraminifera chamber. (B) Image showing multiple medium-size organic-matter pores (bubble pores) in foraminifera chambers. Note the irregular pore on the right side of the lower chamber marked by an arrow that seems to have formed through the amalgamation of smaller spherical pores. (C) High magnification image showing a few medium-size organic-matter pores (bubble pores) and many of the smaller less equant organic-matter pores (spongy pores). This organic matter is bitumen within a coccolith-rich lens. Note that smaller pores can be seen intersecting the walls of the medium-size pore at bottom left. (D) Image showing the boundary between an siliceous-argillaceous seam (top) and a coccolith-rich lens (bottom). The siliceous-argillaceous seam has interparticle pores between clay flakes in contrast to the organic-matter pores in the lens.

The smallest of the organic matter pores are termed spongy pores (Loucks and Reed, 2014). These are typically nanometers to 10s of nanometers in diameter (Fig. 9C). It is common to see spongy pores in the walls of larger bubble and early bitumen pores. The larger organic-matter pore types (early bitumen and bubble pores) appear to be connected by the smaller, more numerous, nanometer-scale spongy organic-matter pores. It is hypothesize that spongy pores are caused by the devolatilization of methane from the bitumen.

Because most pores, including early bitumen pores, bubble pores and spongy pores, are present in bitumen, two factors significantly affect the local fine-scale porosity of samples. First, the number of foraminifera chambers that are filled by bitumen varies from area to area and sample to sample and influences the porosity significantly. Second, the number of pellets that are present varies from area to area and from sample to sample. As the original intraparticle pores in the pellets are filled with nanoporous bitumen, this influences the local porosity.

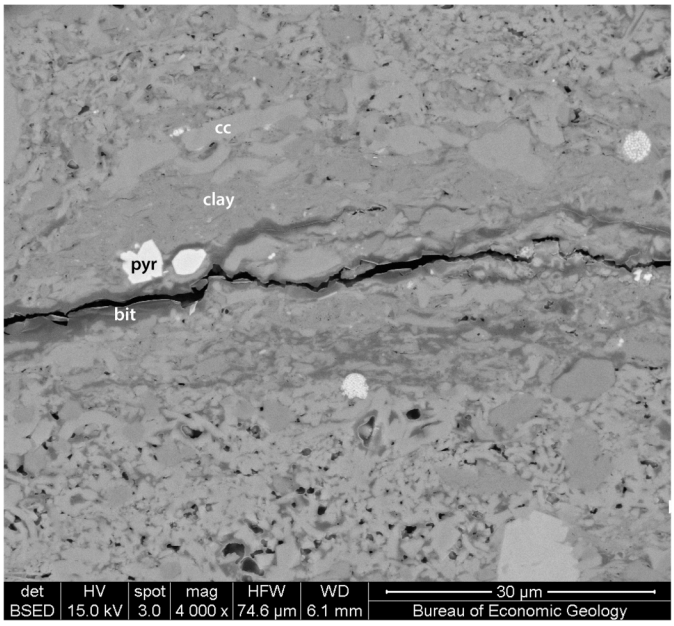

Figure 10. Backscattered electron SEM image of subhorizontal bitumen-filled microfractures. Microfractures have been partially reactivated either during core retrieval or sampling.

The ratio of siliceous-argillaceous seams to pellets varies between samples, influencing the overall pore systems, with the more pellet-rich areas being more porous. There is commonly porosity in the form of organic-matter pores in foraminifera chambers, but it is unclear to what degree these pores are connected to the overall pore system outside the foraminifera.

Geochemical Variation

The variation in foraminifera abundance and chamber fill also affects the chemostratigraphy. This core has been extensively scanned with handheld XRF instruments to map elemental variation. These XRF readings are obtained from a 3 mm oval-shape area. XRF data are commonly used to estimate mineral assemblages in mudrocks (e.g., Algeo et al., 2007). In the samples from this study, the abundance of foraminifera and the ratio of foraminifera fill present in the analysis area seems to be sufficient to alter the bulk chemistry of the sample to a measurable degree in more foraminifera-rich layers; aluminum and silicon values are increased by kaolinite, and calcium values are increased by calcite. Layers with more coccolith-rich pellets will also be higher in calcium. As there is lateral variation in a number of minerals, the horizontal position on a core can also affect XRF spot analyses.

XRF Scans

Some of the patterns visible in the XRF scans (Fig. 3) are better understood when the mineralogy and petrology of the samples are factored in. The most common cause of lamination is variations in the ratio of calcite (coccolith elements and foraminifera tests and fill) versus clay minerals. So, calcium (Fig. 3B) and potassium (Fig. 3D) laminations are driven by these variations. Elements that substitute for calcium in calcite, such as strontium and apparently nickel (Fig. 3H), have similar laminations to calcite. Silicon (Fig. 3C) occurs in both clay minerals and quartz, and the less intense variation between the laminations in the silicon map are influenced by the variety of occurrences of quartz in these samples (detrital grains, recrystallized biogenic silica, quartz cement in foraminifera and radiolarians, and quartz grains of at least partially authigenic origin in coccolith-rich pellets).

The common minerals in these samples that host aluminum (albite, illite, and kaolinite) create the complicated pattern seen in the aluminum XRF scans (Fig. 3E). The strong lamination of clay minerals comes through as only a weak pattern in the aluminum scans. This is driven by the presence of large amounts of kaolinite in foraminifera chambers and the presence of these chambers in otherwise calcite-rich layers. The dispersed nature of the albite also contributes to the weak lamination in aluminum. The highly dispersed distribution of albite may drive the pattern seen in sodium (Fig. 3G), as albite is the primary mineral containing sodium, or as previously noted the sodium pattern may be due to detection problems for light elements.

Magnesium is dominantly in dolomite, and the dolomite occurs both as fill in foraminifera and as matrix grains of various sizes. The wide distribution of dolomite contributes to the generally non-laminated appearance of the magnesium scans.

Titanium lamination most strongly resembles lamination seen in iron (Fig. 3F). Microscopically, titanium occurs in micrometer-scale grains of TiO_2 (unknown which polymorph is present). These grains are found in the siliceous-argillaceous seams, which links titanium with clay mineral occurrence.

Not surprisingly, the distribution of phosphorous is controlled by the occurrence of phosphate, including grains, fossils, and crystals of apatite. The presence of a few high concentration phosphate layers is reflected in the patterns seen in the phosphorous scan. The occurrence of high intensity layers of yttrium that mimic many of the phosphorous layers suggests that yttrium may be substituting into the phosphate structure in some cases.

The distribution of zinc (Fig. 3I) appears to be influenced both by the presence of sphalerite grains observed in the EDS maps and probably some substitution of zinc into clay minerals. This accounts for the combination of dispersed bright spots and a weak lamination that is shown by the zinc scans.

Volcanic Component

Previous workers (e.g., Eldrett et al., 2015; Minisini et al., 2018) have proposed that some of the non-calcareous components of the argillaceous mudstones in the Eagle Ford are volcanic in origin. Arguments for this have been primarily geochemical. This study adds some petrographic evidence to the discussion.

The silt-size euhedral apatite grains that are common in the samples examined for this study, are different than apatite grains seen in other organic-rich mudrock units. In other organic-rich mudrock units, apatite crystals are not nearly as common as they are in these Eagle Ford samples. Also, most apatite crystals from other units show evidence of rounding during transport.

To test a theory regarding the possible source of the apatite crystals, we looked at crystals in the volcanic ash common in the Eagle Ford. However, most available core samples of volcanic ashes had been previously removed for zircon geochronological work (e.g., Pierce et al., 2016; Nieto, 2016). A volcanic ash in core from Karnes County, Texas, was available. The sample is from near the base of the Cretaceous Austin Chalk, at a depth of 11,774.6 ft (3580.7 m), about 12 ft (3.7 m) stratigraphically above the top of the Eagle Ford. This ash is macroscopically similar to ashes seen in the archive portions of Eagle Ford cores. A thin section was made of the Austin ash and it was examined under the SEM. The ash contained euhedral apatite crystals that were similar in size and shape to those seen in the mudrock samples (Fig. 7). These crystals were common in the ash.

Feldspar grains (Fig. 8) are common both in the mudrock and the volcanic ash layer. Both have been albitized and in some cases partially replaced by carbonate (calcite in the ash, dolomite in the mudrock). Grain size of the feldspars in both rock types is coarse silt up to very fine sand. Grain size of the feldspars in the

mudrock are generally larger than that of the detrital quartz grains in the mudrock, suggesting the possibility of different sediment sources.

Quartz grains in the ash layer are mostly silt size and did not have a distinctive shape that would allow them to be recognized in a mudrock layer. Further study of the volcanic quartz, such as cathodoluminescence imaging, might provide definitive characteristics. Zircon grains, an accessory mineral for some volcanic ashes, were not observed in any of the mudrock samples from this study. However, zircons were not common enough to be observed in the thin section of the ash layer either.

Taken together, the similarity of the feldspar and apatite grains suggests that a significant amount of the argillaceous and siliceous material in these samples is sourced from volcanic ash. This raises two possibilities for the source of the volcanic ash. First, the volcanic material could have been delivered slowly as a "dusting" of material over an extended period of time. Or secondly, the ash could have been deposited more rapidly as coherent layer but reworked and mixed into the surrounding sediment by bottom currents. Nieto (2016) found that even thick volcanic ash layers could not always be correlated between closely spaced wells. This would argue for the possibility of extensive localized reworking of Eagle Ford sediments.

This study was limited in scope to one bed of calcareous argillaceous mudstone. It is not known whether volcanic material is commonly mixed into Eagle Ford calcareous sediments or if the studied bed represents an atypical occurrence. Other studies (e.g., Eldrett et al., 2015) have suggested volcanic material is common in Eagle Ford sediments. If much of the "detrital" material in the Eagle Ford (clay minerals, quartz, feldspar, and apatite) is actually volcanic in origin, it would have implications for attempts to tie changes in sediment flux to changes in sea level.

CONCLUSIONS

At the millimeter scale, vertical permeability in the core is negatively affected by grainstone lag laminae, which are rich in calcite cement and have few pores. The number of these grainstone laminae increases toward the toe of the core and thus permeability decreases.

The rock can be divided into three major domains (packages of lithologic components): coccolith-rich pellets, foraminifera, and siliceous-argillaceous seams that wrap the other two domains. The abundance of these domains controls local rock properties. At the micrometer scale, pores vary between abundant organic-matter pores in bitumen-filled coccolith-rich pellets and more sparse interparticle pores that occur in siliceous-argillaceous seams. More pellet-rich areas are more porous.

The variability of foraminifera chamber fill between bitumen, calcite and kaolinite, affects both porosity and geochemistry on a small scale. The presence of more bitumen and kaolinite will increase porosity, whereas calcite mineralization will result in decreased porosity as bitumen and kaolinite are associated with pores. Kaolinite influences silicon and aluminum abundances, and calcite affects calcium abundance. Therefore, XRF data results reflect not only original detrital composition but also the subsequent diagenetic mineralization.

Variation also occurs in minor components of the samples such as albite feldspar, dolomite and phosphatic grains of various types. Differences in the abundance of pyritized radiolarians (originally opaline silica) suggest microscale differences in the amount of dissolved silica available to be precipitated as quartz cement.

The samples contain four different types of organic-matter pores, which vary in size and morphology. Three types occur primarily (bubble and spongy) or exclusively (early bitumen) in bitumen and one type occurs only in kerogen (predepositional).

Both feldspar and euhedral apatite grains in this core are probably volcanic in origin. Much of the non-calcareous component in the samples is probably volcanic in origin rather than terrigenous.

At some point after the consolidation of these rocks, the rocks developed a few open natural subhorizontal microfractures that were subsequently filled with bitumen.

ACKNOWLEDGMENTS

This research was funded by the Mudrock Systems Research Laboratory at the Bureau of Economic Geology, Jackson School of Geosciences, University of Texas at Austin. Sponsoring companies include: Anadarko, Apache, Aramco Services, BHP, BP, Cenovus, Centrica, Chesapeake, Cima, Cimarex, Chevron, Concho, ConocoPhillips, Cypress, Devon, Encana, ENI, EOG, Equinor, EXCO, ExxonMobil, FEI, Geosun, Hess, Husky, IMP, Kerogen, Marathon, Murphy, Newfield, Oxy, Penn Virginia, Penn West, Pioneer, QEP, Repsol, Samson, Shell, Sinopec, Talisman, Texas American Resources, The Unconventionals, University Lands, US EnerCorp, Valence, and YPF. Special thanks is owed to the unnamed company that donated the horizontal core.

Mike Beauchaine and Rebecca Novetsky of Bruker provided results from the M4 Tornado XRF scanning. Harry Rowe supervised acquisition of hand-held XRF data.

Bob Merrill, Stan Paxton, and Chandler Wilhem are thanked for comments on the manuscript. Bob Loucks and Lucy T. Ko are thanked for discussions on the development of organic-matter porosity in the Eagle Ford Group. The Media Group at the Bureau of Economic Geology is thanked for graphics support. Patrick Smith is thanked for assistance with sample preparation. Publication was authorized by the Director, Bureau of Economic Geology, Jackson School of Geosciences, University of Texas at Austin.

REFERENCES CITED

Abrams, M. A., C. Gong, C. Garnier, and M. A. Sephton, 2017, A new thermal extraction protocol to evaluate liquid rich unconventional oil in place and in-situ fluid chemistry: Marine and Petroleum Geology, v. 88, p. 659–675, <https://doi.org/10.1016/j.marpetgeo.2017.09.014>.

Algeo, T. J., R. Hannigan, H. Rowe, M. Brookfield, A. Baud, L. Krystyn, and B. B. Ellwood, 2007, Sequencing events across the Permian-Triassic boundary, Guryul Ravine (Kashmir, India): Palaeogeography, Palaeoclimatology, Palaeoecology, 252, p. 328-346 <https://doi.org/10.1016/j.palaeo.2006.11.050>.

Breyer, J. A., ed., 2016, The Eagle Ford Shale: A renaissance in U.S. oil production: American Association of Petroleum Geologists Memoir 110, Tulsa, Oklahoma, 389 p., <https://doi.org/10.1306/m1101306>.

Dagg, M. J., and W. E. Walser, Jr., 1986, The effect of food concentration on fecal pellet size in marine copepods: Limnology and Oceanography, v. 31, p. 1066–1071, <https://doi.org/10.4319/lo.1986.31.5.1066>.

Denne, R. A., R. E. Hinote, J. A. Breyer, T. H. Kosanke, J. A. Lees, N. Engelhardt-Moore, J. M. Spaw, and N. Tur, 2014, The Cenomanian-Turonian Eagle Ford Group of South Texas: Insights on timing and paleoceanographic conditions from geochemistry and micropaleontologic analyses: Palaeogeography, Palaeoclimatology, Palaeoecology, v. 413, p. 2–28, <https://doi.org/10.1016/j.palaeo.2014.05.029>.

Dunham, R. J., 1962, Classification of carbonate rocks according to depositional texture, *in* W. E. Ham, ed., Classification of carbonate rocks: American Association of Petroleum Geologists Memoir 1, Tulsa, Oklahoma, p. 108–121.

Eldrett, J. S., M. Chao, S. C. Bergman, A. Ozkan, D. Minisini, B. Lutz, S.–J. Jackett, C. Macaulay, and A. E. Kelly, 2015, Origin of limestone–marlstone cycles: Astronomic forcing of organic-rich sedimentary rocks from the Cenomanian to early Coniacian of the Cretaceous Western Interior Seaway, USA: Earth and Planetary Science Letters, v. 423, p. 98–113, <https://doi.org/10.1016/j.epsl.2015.04.026>.

Fairbanks, M. D., S. C. Ruppel, and H. Rowe, 2016, High resolution stratigraphy and facies architecture of the Upper Cretaceous (Cenomanian-Turonian) Eagle Ford Group, Central Texas: American Association of Petroleum Geologists Bulletin, v. 100, p. 379–403, <https://doi.org/10.1306/12071514187>.

Frebourg, G., S. C. Ruppel, R. G. Loucks, and J. Lambert, 2016, Depositional controls on sediment body architecture in the Eagle Ford/Boquillas system: Insights from outcrops in West Texas, United States: American Association of Petroleum Geologists Bulletin, v. 100, p. 657–682, <https://doi.org/10.1306/12091515101>.

Gale, J. F. W., S. E. Laubach, J. E. Olson, P. Eichhubl, and A. Fall, 2014. Natural fractures in shale: A review and new observations: American Association of Petroleum Geologists Bulletin, v. 98, p. 2165–2216, <https://doi.org/10.1306/08121413151>.

Hentz, T. F., W. A. Ambrose, and D. C. Smith, 2014, Eaglebine play of the southwestern East Texas Basin: Stratigraphic and depositional framework of the Upper Cretaceous (Cenomanian-Turonian) Woodbine and Eagle Ford: American Association of Petroleum Geologists Bulletin, v. 98, p. 2551–2580, <https://doi.org/10.1306/07071413232>.

Jarvie, D. M., B. L. Claxton, F. Henk, and J. T. Breyer, 2001, Oil and shale gas from the Barnett Shale, Fort Worth Basin, Texas: American Association of Petroleum Geologists Annual Meeting Program, v. 10, p. A100, <https://doi.org/10.1306/8626e28d-173b-11d7-8645000102c1865d>.

Ko, L. T., R. G. Loucks, S. C. Ruppel, T. Zhang, and S. Peng, 2017, Origin and characterization of Eagle Ford pore networks in the South Texas Upper Cretaceous Shelf: American Association of Petroleum Geologists Bulletin, v. 101, p. 387–418, <https://doi.org/10.1306/08051616035>.

Lash, G. G., and T. Engelder, 2005, An analysis of horizontal microcracking during catagenesis: Example from the Catskill delta complex: American Association of Petroleum Geologists Bulletin, v. 89, p. 1433–1449, <https://doi.org/10.1306/05250504141>.

Loucks, R. G., 2018, Eagle Ford–A depositional setting and processes in southwestern Texas: An example of deeper-water, below-storm-wave-base carbonate sedimentation on a drowned shelf: Gulf Coast Association of Geological Societies Journal, v. 7, p. 59–78, <https://www.gcags.org/Journal/2018.GCAGS.Journal/2018.GCAGS.Journal.v7.04.p59-78.Loucks.pdf>.

Loucks, R. G., and R. M. Reed, 2014, Scanning-electron-microscope petrographic evidence for distinguishing organic-matter pores associated with depositional organic matter versus migrated organic matter in mudrocks: Gulf Coast Association of Geological Societies Journal, v. 3, p. 51–60, <https://www.gcags.org/Journal/2014.GCAGS.Journal/GCAGS.Journal.2014.vol3.p51-60.Loucks.and.Reed.pdf>.

Loucks, R. G., and R. M. Reed, 2016, Natural microfractures in unconventional shale-oil and shale-gas systems: Real, hypothetical, or wrongly defined?: Gulf Coast Association of Geological Societies Journal, v. 5, p. 64–72, <https://www.gcags.org/Journal/2016.GCAGS.Journal/2016.GCAGS.Journal.v5.04.p64-72.Loucks.and.Reed.pdf>.

Loucks, R. G., R. M. Reed, S. C. Ruppel, and U. Hammes, U., 2012, Spectrum of pore types and networks in mudrocks and a descriptive classification for matrix-related mudrock pores: American Association of Petroleum Geologists Bulletin, v. 96, p. 1071–1098, <https://doi.org/10.1306/08171111061>.

Milliken, K. L., 1992, Chemical behavior of detrital feldspars in mudrocks versus sandstones, Frio Formation (Oligocene), South Texas: Journal of Sedimentary Research, v. 62, p. 790–801, <https://doi.org/10.1306/d42679dd-2b26-11d7-8648000102c1865d>.

Milliken, K. L., L. T. Ko, M. Pommer, and K. M. Marsaglia, 2014, SEM petrography of eastern Mediterranean sapropels: Analogue data for assessing organic matter in oil and gas shales: Journal of Sedimentary Research, v. 84, p. 961–974, <https://doi.org/10.2110/jsr.2014.75>.

Milliken, K. L., S. M. Ergene, and A. Ozkan, 2016, Quartz types, authigenic and detrital, in the Upper Cretaceous Eagle Ford Formation, South Texas, USA: Sedimentary Geology, v. 339, p. 273–288, <https://doi.org/10.1016/j.sedgeo.2016.03.012>.

Minisini, D., J. Eldrett, S. C. Bergman, and R. Forkner, 2018, Chronostratigraphic framework and depositional environments in the organic-rich mudstone-dominated Eagle Ford Group, Texas, USA: Sedimentology, v. 65, p. 1520–1557, <https://doi.org/10.1111/sed.12347>.

Nieto, M. A., 2016, Geochronologic and chemostratigraphic record of Cenomanian-Turonian Eagle Ford, South Texas, USA: M.S. Thesis, University of Texas at Austin, 183 p.

Pierce, J. D., S. C. Ruppel, H. Rowe and D. F. Stockli, 2016, Zircon U–Pb geochronology and sources of volcanic ash beds in the Upper Cretaceous Eagle Ford Shale, South Texas. Gulf Coast Association of Geological Societies Journal, v. 5, p. 253–274 <https://www.gcags.org/Journal/2016.GCAGS.Journal/2016.GCAGS.Journal.v5.15.p253-274.Pierce.et.al.pdf>.

Pommer, M., and K. L. Milliken, 2015, Pore types and pore-size distributions across thermal maturity, Eagle Ford Formation, southern Texas: American Association of Petroleum Geologists Bulletin, v. 99, p. 1713–1744 <https://doi.org/10.1306/03051514151>.

Reed, R. M., 2017, Organic-matter pores: New findings from lower-thermal-maturity mudrocks: Gulf Coast Association of Geological Societies Journal, v. 6, p. 99–110, <https://www.gcags.org/Journal/2017.GCAGS.Journal/2017.GCAGS.Journal.v6.07.p99-110.Reed.pdf>.

Reed, R. M., and Ruppel, S. C., 2012, Pore morphology and distribution in the Cretaceous Eagle Ford Shale, South Texas, USA: Gulf Coast Association of Geological Societies Transactions, v. 62, p. 599–604.

Ruppel, S. C., R. G. Loucks, and G. Frébourg, G., 2012, Guide to field exposures of the Eagle Ford-equivalent Boquillas Formation and related Upper Cretaceous units in southwest Texas: Bureau of Economic Geology Mudrock Systems Research Laboratory Field-Trip Guidebook, Austin, Texas, 151 p.

Schieber, J., R. Lazar, K. Bohacs, B. Klimentidis, J. Ottmann, and M. Dumitrescu, 2016, An SEM study of porosity in the Eagle Ford Shale of Texas—Pore types and porosity distribution in a depositional and sequence stratigraphic context: American Association of Petroleum Geologists Memoir 110, Tulsa, Oklahoma, p. 167–186, <https://doi.org/10.1306/13541961m1103589>.